GDCh Research Article Angewandte International Edition Chemie www.angewandte.org

How to cite: *Angew. Chem. Int. Ed.* **2025**, *64*, e202506860
doi.org/10.1002/anie.202506860

Silver Nanoclusters

Solvent-Driven Interconversion of Pyridine Dicarbanion-Bonded Ag_{13} Nanocluster Isomers

Cong Jin, Cui-Cui Li, Kui Xiao, Wan Wang, Songshan Dai, Qianqian Deng, Keting Zhou, Yu Xia, Jun Zhu,* and Liang Zhao**

Abstract: Solvent screening is pivotal for optimizing metal-catalyzed reactions, yet its impact on the in situ formation and reactivity of polynuclear organometallic clusters remains underexplored. We herein isolate two distinct thirteen-membered silver cluster isomers, **Ag_{13}-A** and **Ag_{13}-M**, in acetone and methanol, respectively. Significantly, we demonstrate the interconversion of these isomers facilitated by solvent manipulation. Mechanistic studies on the solvent-driven **Ag_{13}-A** to **Ag_{13}-M** transformation reveal this transformation proceeds with a low activation energy (23.39 ± 0.81 kcal mol^{-1}) and positive entropy, involving counter anion dissociation, ligand twisting, and re-coordination. The observed differences in thermal stability and reactivity between two isomers are attributed to variations in Ag–Ag interactions and surface ligand arrangements, underscoring the critical role of solvent selection in affecting the whole organic transformation through in situ formed clusters. These results highlight the necessity of considering organometallic cluster intermediates in solvent screening.

Introduction

Solvents play a critical role in catalytic reactions by dissolving reactants and catalysts to ensure a homogeneous catalytic environment. The choice of solvent exerts significant influence over reaction rates, equilibriums, and selectivity by tailoring the energy level of intermediates or the energy barrier of transition states through the variation of solvent polarity,[1–4] or direct interaction with reactants.[5–9] In metal-catalyzed reactions, solvent molecules are often considered as temporary ligands to bind with a catalytic metal center, thus affecting its coordination geometry, substrate affinity, and redox property.[7] Accordingly, the solvent screening process is a key step in the optimization of reaction conditions for a wide range of metal-catalyzed reactions aiming at better reaction selectivity and higher yields.

On the other hand, recent mechanistic studies on many metal-catalyzed reactions have revealed that single metal coordination catalysts may undergo reduction by reactants, ligands, or solvents, to in situ form high nuclearity metal clusters or nanoclusters.[10–15] These clusters serve as a dormant state of catalytic species or a temporary reservoir for reactive intermediate species[16–19] to influence reaction kinetics.[20,21] More importantly, they may act as true catalytic species to profoundly influence reaction efficiency and selectivity[13–15] In this regard, solvents possibly affect the size,[22] conformation[23] and peripheral ligand arrangement of in situ formed metal cluster species, thereby substantially altering the whole catalytic process. For example, nanoparticles generated in a cobalt-catalyzed hydrogenation reaction of nitriles can easily regulate their morphologies in different solvents, finally promoting the reaction selectivity to achieve a strong preference for a major product.[23] However, owing to the transient and highly reactive nature of those in situ formed cluster intermediates,[24–28] to date little is known about how solvents influence and determine their structural details. Correlation of solvent-driven structural transformations of in situ formed metal clusters with their reactivity will enable us to obtain a cdeeper understanding and comprehensive elucidation of metal-catalyzed reaction mechanisms (Scheme 1). Recently, some solvent-induced transformations of coinage metal nanoclusters have been reported.[29,30] Though these investigations shed light on the remarkable effect of solvents on the structure and property of metal nanoclusters,[31–35] microscopic factors functioning in the transformation process of metal clusters have been less studied.

[*] C. Jin, K. Xiao, W. Wang, K. Zhou, Y. Xia, L. Zhao
Key Laboratory of Bioorganic Phosphorus Chemistry & Chemical Biology (Ministry of Education), Department of Chemistry, Tsinghua University, Beijing 100084, China
E-mail: xiayu@mail.tsinghua.edu.cn
zhaolchem@mail.tsinghua.edu.cn

C.-C. Li
SINOPEC (Beijing) Research Institute of Chemical Industry Co., Ltd., Yanshan Branch, Beijing 102500, China

S. Dai, Q. Deng
State Key Laboratory of Physical Chemistry of Solid Surfaces, Fujian Provincial Key Laboratory of Theoretical and Computational Chemistry, Department of Chemistry, College of Chemistry and Chemical Engineering, Xiamen University, Xiamen 361005, China

J. Zhu
School of Science and Engineering, The Chinese University of Hong Kong, Shenzhen, Guangdong 518172, China
E-mail: jun.zhu@cuhk.edu.cn

Additional supporting information can be found online in the Supporting Information section

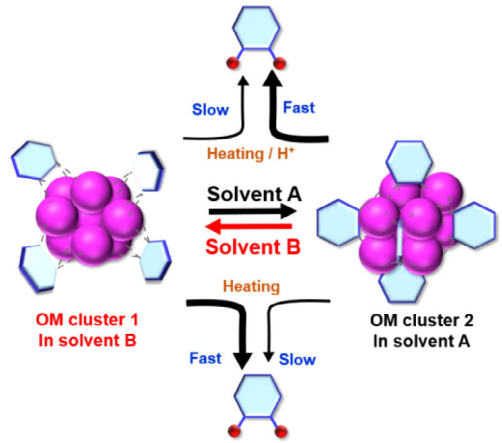

Scheme 1. Interconverted organometallic clusters formed in different solvents.

In this work, two vicinal dicarbanion-bonded Ag_{13} nanocluster isomers were isolated in different solvents, namely, $[Ag_{13}(^{Me}Py–H)_6(CF_3SO_3)_5](CF_3SO_3)$ in acetone (**Ag_{13}-A**) and $([Ag_{13}(^{Me}Py–H)_6(CF_3SO_3)_6]$ in methanol (**Ag_{13}-M**) (^{Me}Py-H = N-H 2-methylpyridyl-4,5-diide). **Ag_{13}-M** features a more regular cuboctahedral core configuration but weaker argentophilic interactions relative to **Ag_{13}-A**. For the first time, we observed a solvent-induced interconversion between two sp^2-carbon-bonded organometallic cluster isomers. Its relatively low activation energy of 23.39 ± 0.81 kcal mol^{-1} suggests an unconventional ligand twist mechanism. Further experimental and theoretical studies confirm that the transformation involves a solvent-induced dissociation of coordinated anions, followed by spatial tuning of partial pyridine dicarbanion ligands and recombination of anions. **Ag_{13}-M** shows poor stability upon heating, in sharp contrast to the well-maintained **Ag_{13}-A** at an elevated temperature. However, in acidic solution **Ag_{13}-M** exhibits sluggish reactivity due to less negative charges on the carbanionic sites relative to **Ag_{13}-A**. Structural examination and reactivity studies on these unprecedented organometallic nanocluster isomers demonstrate a new perspective on solvent dependency in metal-catalyzed organic transformations beyond solubility and auxiliary coordination.

Results and Discussion

Synthesis and Structural Characterization of Ag_{13} Nanocluster Isomers

In our previous work,[36] a silver(I)-mediated intermolecular annulation reaction of methyl ketones and propargylamine was performed in the presence of excessive silver salts and a polydentate macrocyclic ligand octamethylazacalix[8]pyridine (Py[8]). The following continuous multi-step transformation of condensation, imine–enamine isomerization, 6-*endo-dig* cyclization, and oxidative aromatization yielded a series of substituted pyridyl dicarbanion bonded Ag_4 clusters, for example **^{Me}PyAg$_5$** as shown in Scheme 2. Addition of triflic acid CF_3SO_3H (HOTf) to the acetone solution of **^{Me}PyAg$_5$** allowed the removal of the peripheral ligand Py[8] and finally yielded both colorless needle-like (13% crystal yield) and brown block-shaped crystals (52% yield). The colorless compound was determined by single crystal X-ray diffraction (SCXRD) as protonated 2,2′-dimethyl-4,4′-bipyridine, which is derived from the protonlysis and oxidative coupling of pyridine dicarbanions. Surprisingly, the brown crystalline compound was found actually a 13-membered silver nanocluster **Ag_{13}-A** *vide infra*. In contrast, upon the use of methanol as solvent, a similar acidification and crystallization process led to brown rod-like crystals of a new silver cluster compound **Ag_{13}-M** in a relatively low yield of 13%, together with colorless protonated 2,2′-dimethyl-4,4′-bipyridine in 54% crystal yield (Scheme 2).

Electrospray ionization mass spectroscopy (ESI-MS) characterization of the brown crystalline sample **Ag_{13}-M** gave two well-resolved isotopic peaks at m/z = 2847.8011 and 2865.7853 (Figure S3), which can be assigned as $\{[Ag_{13}(^{Me}Py-H)_6](CF_3SO_3)_6\}^+$ and $\{[Ag_{13}(^{Me}Py-H)_6](CF_3SO_3)_6\cdot H_2O\}^+$. This result confirms the same atomic composition of **Ag_{13}-M** with **Ag_{13}-A** (m/z = 2847.7750 and 2865.7704). In contrast to four aromatic proton peaks observed in the ^{1}H-NMR spectrum of **Ag_{13}-A** (8.89, 8.28–8.19, and 7.98 ppm in a ratio of 1 : 10 : 1, Figure S4a), **Ag_{13}-M** exhibits only two sets of peaks for aromatic protons (8.22 and 8.11 ppm in a ratio of 1:1, Figure S4b). Such NMR signal discrepancy suggests that **Ag_{13}-M** possibly owns a higher symmetry than **Ag_{13}-A**. In addition, the well-defined ESI-MS and NMR signals indicate that **Ag_{13}-A** and **Ag_{13}-M** nicely maintain their structural integrity in solutions.

SCXRD analysis of **Ag_{13}-A** reveals a three-layered twisted cuboctahedral Ag_{13} core (Ag_3–Ag_7–Ag_3) that has a dihedral angle of 9.7° between two Ag_3 layers. Except for a free $CF_3SO_3^-$ counter anion, this silver cluster core is peripherally wrapped by six N-protonated 2-methylpyridyl-4,5-diides via a μ_4-C,C-η^2,η^2 mode and five μ_2-O,O-η^1,η^1 coordinated triflates (Figure 1a). Among the five coordinated triflates, three of them surround the central Ag_7 layer, while the remaining two connect with an edge of the upper Ag_3 plane and an interplanar Ag_3–Ag_7 edge, respectively. In contrast, **Ag_{13}-M** shows a similar but more regular cuboctahedral Ag_{13} core, which has a high symmetry of R-3 and is peripherally decorated by six ^{Me}Py-H ligands as well. Notably, six μ_2-O,O-η^1,η^1 triflate groups in **Ag_{13}-M** are all bonded with the central Ag_7 plane in an alternate way (Figure 2d). Furthermore, the total 36 Ag–Ag connections in both **Ag_{13}-A** and **Ag_{13}-M** can be classified into three types (highlighted in blue, green, and red colors in Figure 1c,f). The average Ag–Ag distance between the central silver atom and the surrounding twelve silver ions in **Ag_{13}-M** is 3.014 Å (blue in Figure 1c and Figure S5), which is longer than the mean value of **Ag_{13}-A** (2.970 Å, blue in Figure 1f and Figure S5). Among the 24 peripheral Ag–Ag sides, the average distance of the shorter μ_2-C-bridging Ag–Ag sides (red in Figure 1c,f) in **Ag_{13}-M** and **Ag_{13}-A** is comparable (2.747 and 2.755 Å, respectively). However, the μ_2-C,C-bridging Ag–Ag edges in **Ag_{13}-M** have an average distance of 3.268 Å, longer than the value of 3.177 Å in **Ag_{13}-A** (green in Figure 1c,f). In addition, the

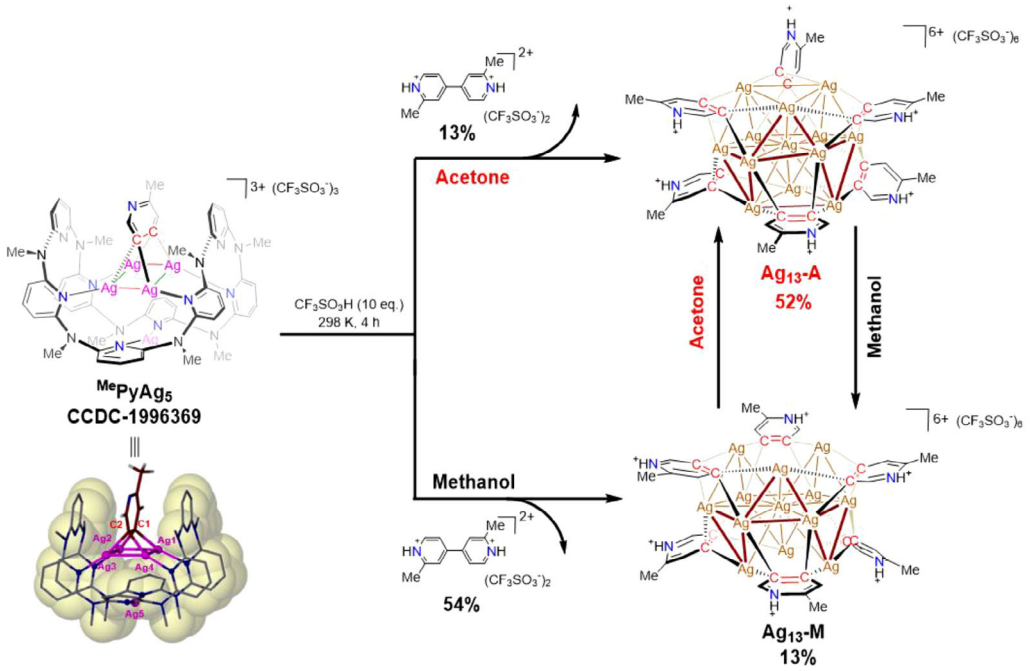

Scheme 2. Synthetic procedure and transformation of two nanocluster isomers **Ag_{13}-A** and **Ag_{13}-M**.

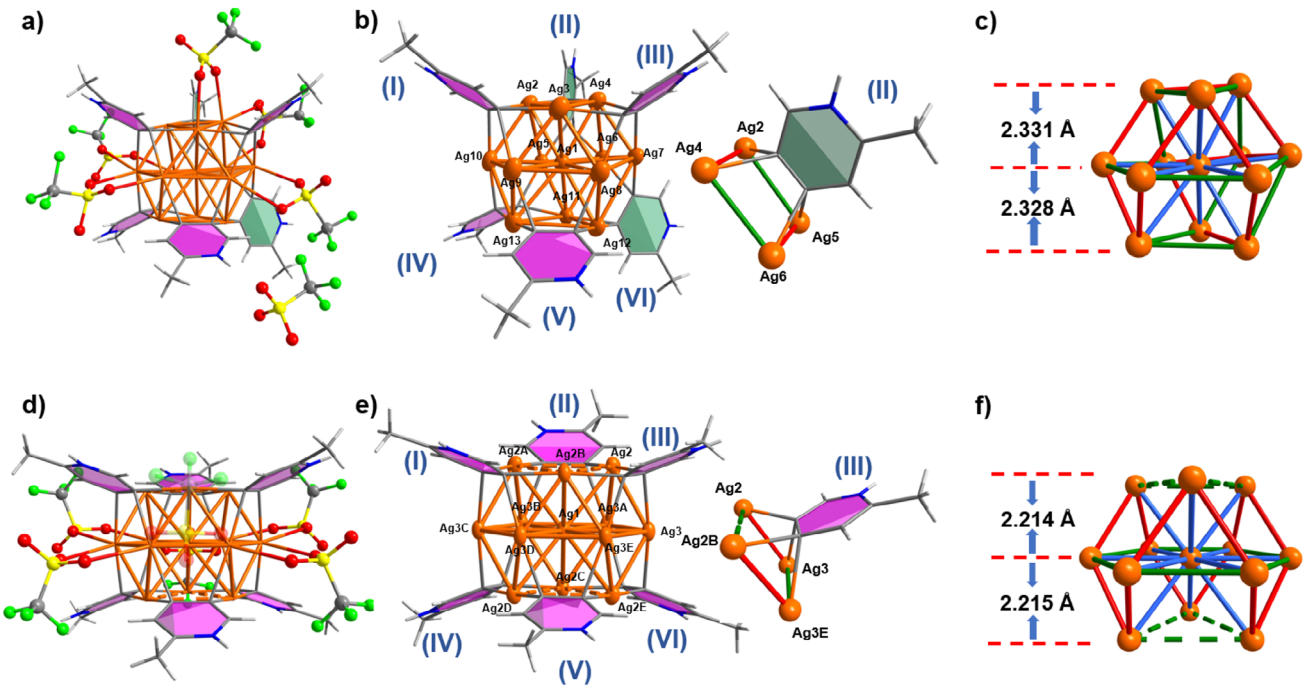

Figure 1. Crystal structures of a–c) **Ag_{13}-A** and d–f) **Ag_{13}-M**. Five coordinated counter anions and one free triflate anion are shown in **Ag_{13}-A** (a) and all six coordinated ones are included in **Ag_{13}-M** (d). Equatorial and vertical arrangements of the 2-methylpyridine rings attached on the Ag_{13} kernel are shown in purple and light green color, respectively, in (b) **Ag_{13}-A** and (e) **Ag_{13}-M**. Thermal ellipsoids of Ag atoms are set at 50% probability level. Different kinds of Ag–Ag interaction (below 3.4 Å) are shown in colored lines in the Ag_{13} core of (c) **Ag_{13}-A** and (f) **Ag_{13}-M**. Blue: central Ag1 with surrounding Ag atoms; red: the μ_2-C-bridging Ag–Ag edges; green: the μ_2-C,C-bridging Ag–Ag edges. Color code for atoms: orange, Ag; gray, C; white, H; blue, N; yellow, S; red, O; green, F.

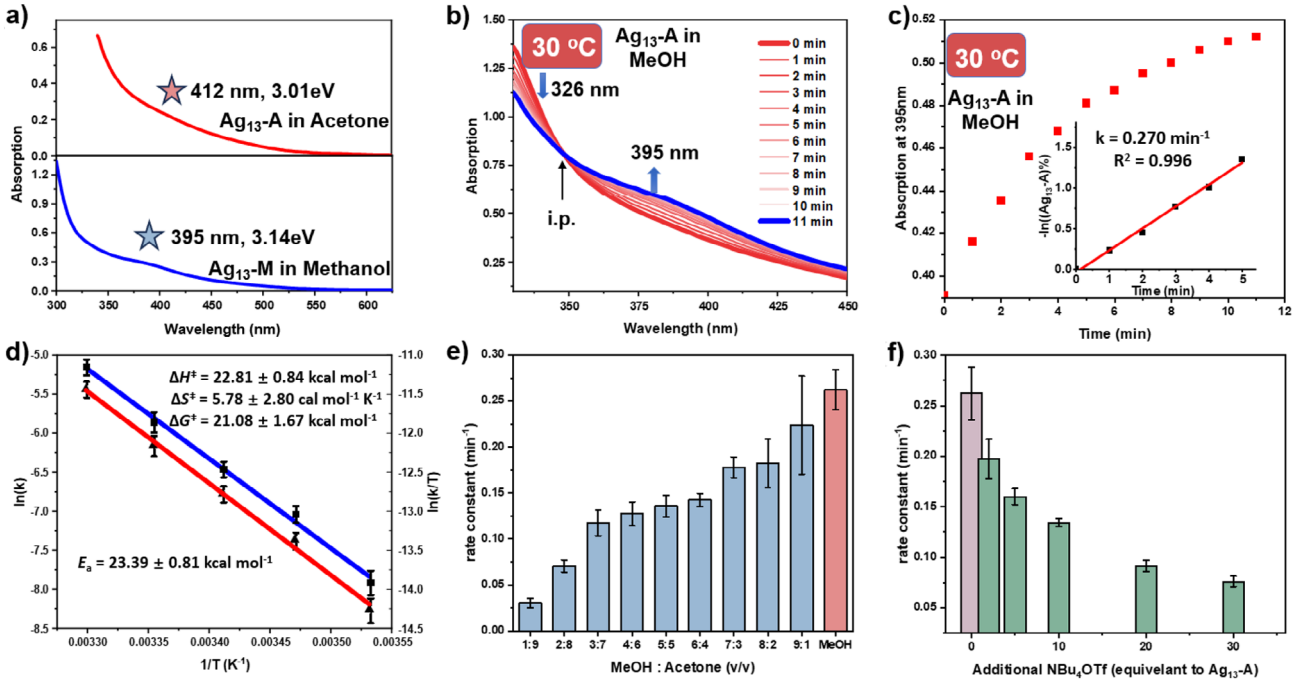

Figure 2. a) UV–vis absorption spectra of **Ag_{13}-A** in acetone and **Ag_{13}-M** in methanol with characteristic absorption peaks. The cut-off wavelength of **Ag_{13}-A** was set as 340 nm due to strong absorption of acetone below 340 nm. b) Time-dependent UV–vis absorption spectral monitoring on the **Ag_{13}-A** to **Ag_{13}-M** transformation in methanol at 30 °C. i.p.: isosbestic point (340 nm). c) Fitting to the first-order reaction kinetic for the **Ag_{13}-A** to **Ag_{13}-M** transformation in methanol based on the absorption at 395 nm. d) The Arrhenius (red line, left axis, $R^2 = 0.996$) and Eyring plots (blue line, right axis, $R^2 = 0.996$) for the **Ag_{13}-A** to **Ag_{13}-M** transformation (10, 15, 20, 25, and 30 °C). e) Rate constants for the **Ag_{13}-A** to **Ag_{13}-M** transformation in mixed MeOH-acetone solutions (v/v: 1:9 to 10:0) (30 °C). f) Rate constants for the **Ag_{13}-A** to **Ag_{13}-M** transformation in methanol upon the addition of different equivalents NBu_4OTf (30 °C).

Ag_{13} core in **Ag_{13}-M** is severely squashed with a mean interplanar distance of 2.214 Å between the central Ag_7 and the upper and lower Ag_3 layers (Figure 1f), which are smaller than **Ag_{13}-A** (2.331 and 2.328 Å, Figure 1c). This structural difference may be ascribed to the presence of 12 μ_2-C-Ag_2 connections bridging the Ag_3 layers and the equatorial Ag_7 plane in **Ag_{13}-M**, but only eight ones in **Ag_{13}-A**. In addition, the Ag–Ag distances in the upper and lower Ag_3 planes of **Ag_{13}-M** (dashed green lines) are 3.512 Å, which exceeds the sum of the van der Waals radii of silver atom (3.4 Å).[37] The above structural analysis clearly shows that the Ag–Ag interactions in **Ag_{13}-M** are weaker than in **Ag_{13}-A** (Figure S5). On the other hand, six ^{Me}Py-H ligands in **Ag_{13}-M** all occupy the equatorial position with a propeller-like C_3 symmetry (Figure 1e). This spatial arrangement is different from the scenario of four equatorial and two vertical protonated 2-methylpyridyl diides on the cluster surface of **Ag_{13}-A**. Furthermore, the average C—Ag bond lengths in the two isomers are comparable (2.222 Å in **Ag_{13}-A** and 2.226 Å in **Ag_{13}-M**) but with different variances. The C—Ag bonds of **Ag_{13}-M** formed between the dicarbanion and the central Ag_7 layer (average ~2.305 Å) are significantly longer than those connected with the upper and lower Ag_3 layers (average ~2.153 Å). This unsymmetrical bonding should be ascribed to the steric hindrance from six coordinated triflates attached on the waist position of Ag_{13}. In contrast, the C—Ag bond lengths in **Ag_{13}-A** show relatively uniform distribution. The C—Ag bond lengths for vertical ^{Me}Py-H ligands span the range from 2.143 to 2.287 Å, which is comparable with the range for the equatorial ligands (2.132–2.317 Å).

Solvent-Driven Interconversion between Ag_{13}-A and Ag_{13}-M

Considering the structural and synthetic similarity between **Ag_{13}-A** and **Ag_{13}-M**, we further investigated the possibility of solvent-induced structural transformation. The UV–vis spectra of two structural isomers in methanol and acetone both exhibit a wide absorption range from 300 to 500 nm. Notably, there are characteristic shoulder peaks at 412 nm for **Ag_{13}-A**, and 395 nm for **Ag_{13}-M** (Figure 2a), which make it feasible to employ UV–vis monitoring to track their structural transformation. After dissolving **Ag_{13}-A** in a minimal amount of acetone and subsequently adding it to a methanol solution, we observed a gradual decrease of the characteristic absorbance of **Ag_{13}-A** at 326 nm, which was accompanied with the stepwise increase of the featured absorbance of **Ag_{13}-M** at 395 nm (Figure 2b). Furthermore, the presence of an isosbestic point at 340 nm suggests an equilibrium-based conversion process between such two cluster isomers. Upon the addition of **Ag_{13}-M** into acetone, the characteristic absorption of **Ag_{13}-A** at 412 nm gradually increased despite that this **M**-to-**A** transformation process needs a much longer time of 2 h (Figure S10). Furthermore, after the forward rapid **A**-to-**M** and reverse sluggish

M-to-**A** solvent-driven conversions, we isolated corresponding structural isomers as crystalline solids, which are suitable for SCXRD.

In view of the slow **M**-to-**A** transformation in acetone, our further kinetic studies laid attention on the **A**-to-**M** transformation in methanol. As shown in Figure 2c, the UV–vis spectral monitoring on the absorption at 395 nm for the **A**-to-**M** transformation is fitted nicely to a first-order reaction kinetic.[38] Variable temperature reaction rate measurements show a good linear fitting to the Arrhenius and Eyring equations (Figure 2d). According to the Arrhenius plot, the activation energy (E_a) is determined as 23.39 ± 0.81 kcal mol^{-1}. The Eyring plot shows the enthalpy, entropy, and Gibbs free energy of activation as $\Delta H^{\ddagger} = 22.81$ ± 0.84 kcal mol^{-1}, $\Delta S^{\ddagger} = 5.78 \pm 2.80$ cal mol^{-1} K^{-1}, and $\Delta G^{\ddagger} = 21.08 \pm 1.67$ kcal mol^{-1}, respectively. The positive activation entropy implies that the transformation process may experience a dissociation of the $[Ag_{13}(^{Me}Py–H)_6(CF_3SO_3)_5]^+$ cluster moiety in **Ag_{13}-A**.

We further studied the role of alcohol solvents in the cluster transformation by measuring rate constants in mixed solvents of methanol and acetone. As shown in Figure 2e, along with the increase of methanol content, rate constants for the **A**-to-**M** transformation accelerate accordingly and finally achieve the maximum speed in pure methanol (0.262 ± 0.0213 min^{-1}). Besides the solvent effect, we found that counter anions also play an important role in the cluster transformation. Upon increasing tetrabutylammonium triflate (NBu_4OTf) in the methanol solution of **Ag_{13}-A** (Figure 2f), the rate constant for the **A**-to-**M** transformation was greatly inhibited by triflates. This trend aligns with the above positive activation entropy $\Delta S^{\ddagger}$, suggesting that the transformation process entails a temporary dissociation of coordinated counter anions. Clearly, this dissociation causes the generation of charged species, which is favorably stabilized in polar solvents (e.g., methanol).

To further investigate microscopic contributions of solvent molecules during cluster transformations, we determined the activation parameters for the **A**-to-**M** transformation in a series of MeOH/acetone mixed solvents with varying volume ratios (Figure 3 and Table S2). The results reveal that both E_a and $\Delta H^{\ddagger}$ undergo a V-shaped variation along with the increase of methanol portion in mixed solvents. Notably, in all mixed solvent compositions, $\Delta S^{\ddagger}$ values are negative and reach a minimum value of −25.89 ± 2.82 cal mol^{-1} K^{-1} in the 5:5 MeOH-acetone mixture, in sharp contrast to the positive value in pure methanol (5.78 ± 2.80 cal mol^{-1} K^{-1}). The consistent and almost unchanged $\Delta G^{\ddagger}$ (21.40 ± 0.38 kcal mol^{-1}) in different mixed solvents and methanol may be attributed to the linear enthalpy–entropy compensation effect.

To rationalize the acquired activation parameters in MeOH/acetone mixed solvents, we attempt to separately consider solvent–solvent and solvent–solute interactions.[39–41] Given the presence of protonated pyridines in the surrounding ligands, hydrogen bonding between those protonated pyridines and solvent molecules must be considered as well. As the volume ratio of methanol increases from 1:9 to 5:5,

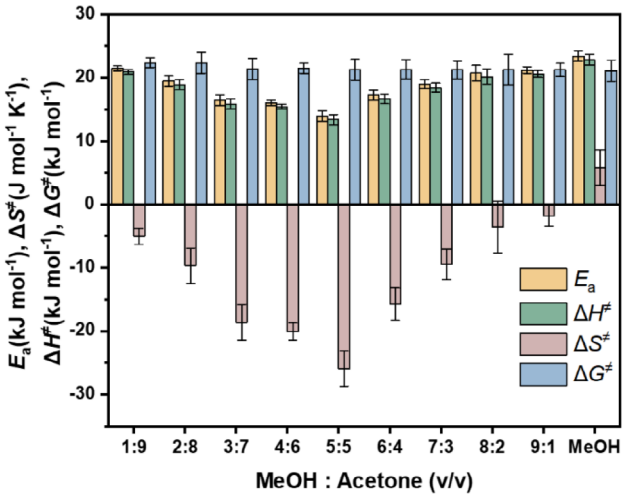

Figure 3. Activation parameters for the **Ag_{13}-A** to **Ag_{13}-M** transformation in mixed solvents of MeOH/acetone(v/v) and methanol.

hydrogen bonding between methanol and the protonated pyridine ligands favorably stabilizes the transition state in the **A**-to-**M** transformation, therefore reducing the activation energy (E_a) and the activation enthalpy ($\Delta H^{\ddagger}$). However, when the methanol ratio further increases up to 9:1 or even pure methanol, the dominant interaction shifts to the formation of a hydrogen-bonding network by methanol itself. This reduces the solvation effect on the silver cluster, and the hydrogen bonding between the cluster transition state and methanol has to compensate for the energy required to break the intrinsic methanol-based hydrogen-bonding network. Consequently, both the activation energy and activation enthalpy increase. Meanwhile, strong solvation leads to a highly ordered arrangement of solvent molecules around the solute by forming a solvent shell, resulting in a negative activation entropy ($\Delta S^{\ddagger}$).[42] Additionally, solvent molecules surrounding the transition state may hinder the rotation of surface ligands, leading to a decrease in reaction rates.

The straightforward **A**-to-**M** transformation in methanol was further rationalized by theoretical studies. In methanol, the single-point energy of **Ag_{13}-M** is 23.1 kcal mol^{-1} lower than that of **Ag_{13}-A** (Figure 4a). This energy difference can be attributed to a larger dipole moment of **Ag_{13}-M** relative to **Ag_{13}-A**. Considering the similar Ag_{13} core in such two isomers, we calculated the contribution of six ligands to the dipole moment, which is 7.737 a.u. for **Ag_{13}-M** and 3.495 a.u. for **Ag_{13}-A** (Figure S13). As a result, **Ag_{13}-M** with a relatively large dipole moment is plausibly more stable than **Ag_{13}-A** in polar solvents, providing a driving force for the **A**-to-**M** transformation. When the implicit solvent model is changed to acetone, **Ag_{13}-A** and **Ag_{13}-M** show a similar energy level (Figure 4b), the driving force for the **M**-to-**A** transformation is primarily provided by acetone coordination (Figure S11).

On the other hand, structural comparison between **Ag_{13}-A** and **Ag_{13}-M** suggests that the **A**-to-**M** transformation must experience a spatial arrangement of two 2-methylpyridyl

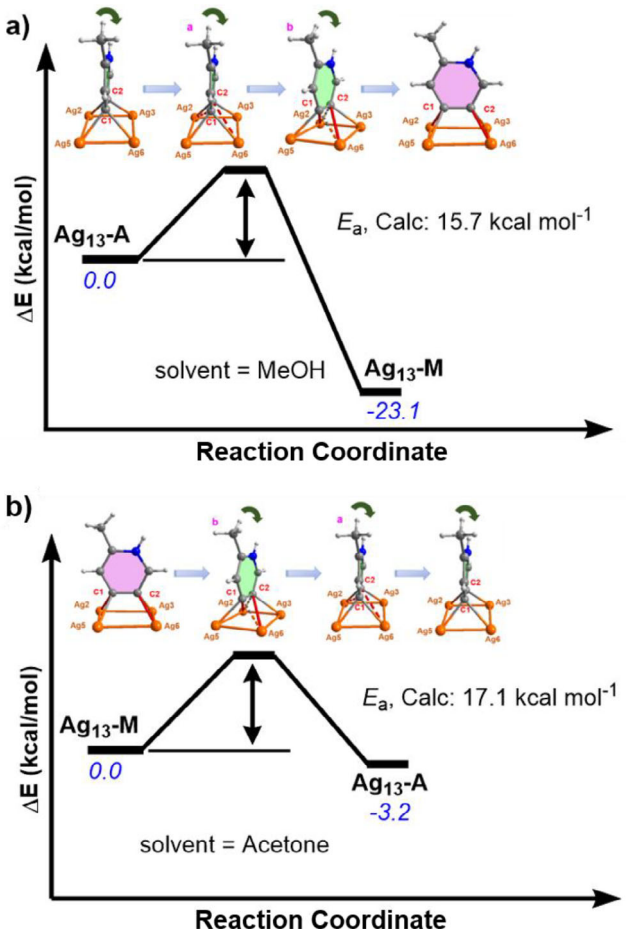

Figure 4. Single-point energy calculations and proposed mechanism for a) the vertical to equatorial spatial rearrangement of a ^{Me}Py-H diide ligand in the **A**-to-**M** transformation and b) the equatorial to vertical rearrangement in the **M**-to-**A** transformation. Energy calculations for the **M**-to-**A** transformation involve the coordination of acetone molecules (Figure S11 and Table S3). Computed at the PBE0-D3/Def2-SVP level with SMD model in MeOH or Acetone.

diides from vertical to equatorial positions. However, the relatively low measured activation energy E_a of 23.39 ± 0.81 kcal mol^{-1} for the **A**-to-**M** transformation implies that this process may not involve the dissociation and recombination of 2-methylpyridyl diide ligands. Previous racemization process studies on a chiral thiolate-protected nanocluster $Au_{38}(SCH_2CH_2Ph)_{24}$ have revealed a structural rearrangement mechanism, which involves a place exchange of thiolates without breaking Au–S bonds on the cluster surface (experimental activation energy E_a = 28 kcal mol^{-1}).[43] We thus propose a twist mechanism for the **A**-to-**M** transformation, as shown in Figure 4a. First, a few coordinated $CF_3SO_3^-$ counter ions dissociate from the Ag_{13} core of **Ag_{13}-A**. Then, the vertically coordinated ^{Me}Py-H diide ligand attached on a tetrasilver plane undergoes a twist and slide motion to change its orientation to the equatorial position. Finally, the separated $CF_3SO_3^-$ ions re-coordinate with the Ag_{13} cluster core to form **Ag_{13}-M**. This ligand twist mechanism was supported by DFT calculation. The twist barrier for the **M**-to-**A** transformation under an implicit

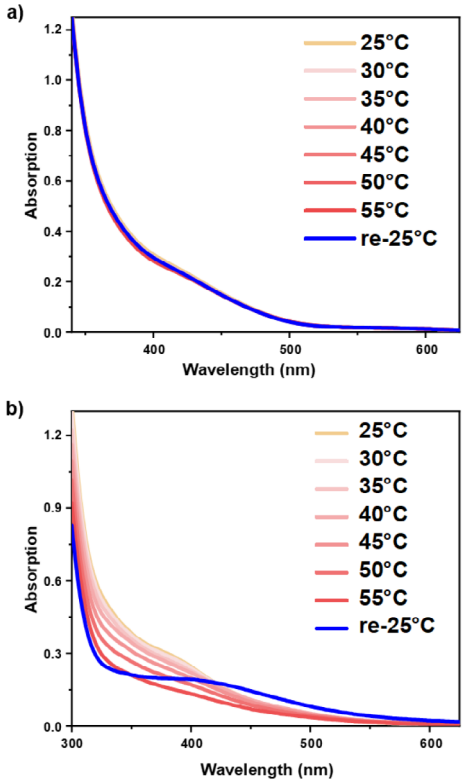

Figure 5. In situ UV–vis spectral monitoring on the thermal stability of a) **Ag_{13}-A** in acetone and b) **Ag_{13}-M** in methanol from 25 to 55 °C.

acetone solvation model is approximately 1.4 kcal mol^{-1} (ΔE_a) higher than the **A**-to-**M** barrier, which may account for the slow **M**-to-**A** transformation.

Stability and Reactivity Studies of Ag_{13}-A and Ag_{13}-M

In order to clarify the role of these organometallic intermediates in metal-catalyzed reactions, we further evaluated the stability and reactivity of **Ag_{13}-A** and **Ag_{13}-M**. As the temperature increased from 25 to 55 °C by half an hour, the UV–vis spectra of **Ag_{13}-A** in acetone displayed negligible changes (Figure 5a). In contrast, the same heating process for the methanol solution of **Ag_{13}-M** led to a remarkable decrease of the characteristic absorbance at 395 nm. Finally, a new absorption band appeared in a wide range of 350–500 nm (Figure 5b). In view of the characteristic UV–vis absorption band in the range of 400–500 nm for silver nanoparticle samples,[44] we conceive that the heating process may destruct **Ag_{13}-M** and subsequently facilitate the formation of silver nanoparticles. The better thermal stability of **Ag_{13}-A** over **Ag_{13}-M** should be attributed to the relatively stronger Ag–Ag interactions in **Ag_{13}-A** *vide supra*.

We then monitored the heating process of **Ag_{13}-M** by ^{1}H NMR to identify the resulting products. After heating **Ag_{13}-M** in d_4-methanol at 50 °C for 2 h, the peaks corresponding to **Ag_{13}-M** totally disappeared. Meanwhile, two sets of new peaks appeared in the aromatic region, which remained unchanged thereafter (Figure S15). Based on

further structural characterization by ESI-MS (Figure S17), ^{1}H NMR (Figure S18), and SCXRD (Figure S19), we assigned the resulting products as a protolysis compound 2-methylpyridine (abbreviated as ^{Me}Py, yield 69%) and a hydroxylated compound 2-methylpyridin-3-ol (abbreviated as (OH)^{Me}Py, yield 24%). We also conducted the same heating experiment on **Ag_{13}-A** in d_6-acetone. Due to better thermal stability of **Ag_{13}-A**, its cluster signals disappeared after 4 h of heating at 50 °C (Figure S16). The resulting products were identified as ^{Me}Py (63%) and (OH)^{Me}Py (21%) as well. It has been reported that 2-methylpyridine can be converted to 2-methylpyridin-3-ol by $Cu(NO_3)_2$ and H_2O_2.[45] We conjecture that the formation of the hydroxylated product arises from a radical-based mechanism involving homolytic cleavage of the Ag–C bond and an intramolecular radical transfer reaction. This assumption was supported by a radical capture experiment. Along with the addition of a radical scavenger (2,2,6,6-tetramethylpiperidine-*N*-oxyl, TEMPO) in the heated solution of **Ag_{13}-A**, we observed an adduct of TEMPO and ^{Me}Py-H rather than (OH)^{Me}Py in high-resolution mass spectrometry (Figure S22). In addition, we incorporated ^{18}O-labeled H_2O and O_2 in reaction conditions to conduct the thermal decomposition of **Ag_{13}-A**. The absence of ^{18}O-labeled (OH)^{Me}Py in mass spectrum implies that the source of oxygen in (OH)^{Me}Py is likely from the counter anion OTf^-.[46]

We further investigated the reactivity of the two isomers in the presence of acid at 50 °C, which is motivated by the isolation of the protolysis product ^{Me}Py. Moreover, the protolysis of carbon–metal bonds is often the final step in many metal-catalyzed reactions, which facilitates the release of active metal species to renew the catalytic cycle.[18,19] However, both two Ag_{13} isomers counterintuitively showed enhanced stability in acidic solutions. Upon the addition of 10 equivalents of HOTf to the methanol solution of **Ag_{13}-M**, it took 80 h at 50 °C to completely destruct **Ag_{13}-M** as monitored by ^{1}H NMR. As to **Ag_{13}-A** in acetone, seven-hour heating at 50 °C was required to complete the protolysis and hydroxylation reaction (Figures S21 and S22). Further comparative experiments with the addition of 10 equivalents of non-coordinated HBF_4 or 10 equivalents of NBu_4OTf showed that the proton abundance is responsible for the enhanced cluster stability (Figure S23). In view of the protonated form of 2-methylpyridine diide in both **Ag_{13}-A** and **Ag_{13}-M**, we believe that the added acid inhibits the proton dissociation from the pyridyl nitrogen atom. As a consequence, the steady protonation decreases the electron density of pyridine ligands and C–Ag bonding. The balance of diminished C–Ag bond reactivity and enhanced solution acidity promotes the stabilization of the clusters. After the destruction experiment by heating, the acidic solutions of **Ag_{13}-A** and **Ag_{13}-M** produce the same products ^{Me}Py and (OH)^{Me}Py in comparable yields (Table 1). To explain the reluctant reactivity of **Ag_{13}-M** (80 h at 50 °C) relative to **Ag_{13}-A** (7 h at 50 °C) in acidic solutions, we carried out theoretical studies to quantify charge distribution of the pyridyl diide ligands. Atomic Dipole Corrected Hirshfeld (ADCH) analysis showed that the carbanion sites in **Ag_{13}-M** have less negative charge (C_4: −0.0745 and C_5: −0.0462) than that of **Ag_{13}-A** (C_4: −0.176 and C_5: −0.285) (Table S4). This result suggests that the pyridyl dicarbanion sites in **Ag_{13}-M** are less likely to be protonated, thereby maintaining prolonged stability in the acidic solution.

Table 1: Reactivity of Ag_{13} isomers under different conditions.[a]

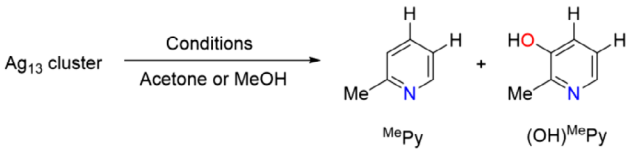

Entry	Cluster	Conditions	Duration of cluster signals	Yield ^{Me}Py	Yield (OH)^{Me}Py
1	**Ag_{13}-M**	50 °C	2 h	69%	24%
2	**Ag_{13}-M**	50 °C with 10eq HOTf	80 h	64%	32%
3	**Ag_{13}-A**	50 °C	4 h	63%	21%
4	**Ag_{13}-A**	50 °C with 10eq HOTf	7 h	66%	29%

[a] Reaction conditions: Ag_{13} clusters (0.001 mmol), **Ag_{13}-M** in d_4-methanol or **Ag_{13}-A** in d_6-acetone (0.55 mL) at 50 °C in a seal tube. The yields were determined by ^{1}H NMR analysis using 1,3,5-tri-tert-butylbenzene as an internal standard.

Conclusion

In conclusion, through the manipulation of solvents, we have successfully isolated two structural isomers of 2-methylpyridyl dicarbanion-bonded organometallic Ag_{13} clusters. Our investigations have elucidated a solvent-induced interconversion process between these Ag_{13} nanocluster isomers, both experimentally and theoretically. This transformation was found to be influenced significantly by temperature, dynamic behavior of anions, and solvent environment. The polarity of methanol is well matched with the large dipole moment of **Ag_{13}-M**, which possibly accounts for the driving force for the **A**-to-**M** transformation in methanol. In contrast, the **M**-to-**A** transformation in acetone is likely driven by the coordination of acetone molecules to the cluster core. Notably, the weakened Ag–Ag interactions and ligand chelation in **Ag_{13}-M** contribute to its comparatively lower thermal stability, although it demonstrates enhanced stability in acidic environments compared to **Ag_{13}-A**, likely due to reduced charge at the dicarbanion sites. The observed solvent-driven interconversion and distinct reactivity profiles of these Ag_{13} nanocluster isomers offer valuable insights into the crucial roles of solvents and mechanistic investigations in metal-catalyzed organic transformations.

Supporting Information

Full characterization data including NMR spectra, high-resolution ESI-MS, UV–vis and crystallographic data, DFT calculations, and experimental details (PDF).

Input coordinates of models (XYZ).

The authors have cited additional references within the Supporting Information.[47–60]

Acknowledgements

Financial support by National Natural Science Foundation of China (22025105, 22350002 and 22074075) is gratefully acknowledged.

Conflict of Interests

The authors declare no conflict of interest.

Data Availability Statement

The data that support the findings of this study are available from the corresponding author upon reasonable request. CCDC 1995296 (**Ag_{13}-A**), 1994912 (**Ag_{13}-M**) and 2344925 (**$(OH)^{Me}$Py-Ag**) contain the supplementary crystallographic data for this paper. These data can be obtained free of charge via www.ccdc.cam.ac.uk/ data_request/cif.

Keywords: Cluster interconversion · Cluster reactivity · Solvent effect

[1] J. Sherwood, J. H. Clark, I. J. S. Fairlamb, J. M. Slattery, *Green Chem.* **2019**, *21*, 2164–2213.
[2] A. Gordillo, M. A. Ortuño, C. López-Mardomingo, A. Lledós, G. Ujaque, E. de Jesús, *J. Am. Chem. Soc.* **2013**, *135*, 13749–13763.
[3] L. Xue, Z. Lin, *Chem. Soc. Rev.* **2010**, *39*, 1692–1705.
[4] F. Proutiere, F. Schoenebeck, *Angew. Chem. Int. Ed.* **2011**, *50*, 8192–8195.
[5] C. Reichardt, *Pure Appl. Chem.* **1982**, *54*, 1867–1884.
[6] R. Jana, T. P. Pathak, M. S. Sigman, *Chem. Rev.* **2011**, *111*, 1417–1492.
[7] E. K. Elias, S. M. Rehbein, S. R. Neufeldt, *Chem. Sci.* **2022**, *13*, 1618–1628.
[8] Y. P. Budiman, A. Jayaraman, A. Friedrich, F. Kerner, U. Radius, T. B. Marder, *J. Am. Chem. Soc.* **2020**, *142*, 6036–6050.
[9] C. Yu, J. Sanjose-Orduna, F. W. Patureau, M. H. Perez-Temprano, *Chem. Soc. Rev.* **2020**, *49*, 1643–1652.
[10] T. N. Gieshoff, U. Chakraborty, M. Villa, A. Jacobi von Wangelin, *Angew. Chem. Int. Ed.* **2017**, *56*, 3585–3589.
[11] V. Lavallo, Y. Canac, A. DeHope, B. Donnadieu, G. Bertrand, *Angew. Chem. Int. Ed.* **2005**, *44*, 7236–7239.
[12] C. H. Li, S. Song, Y. L. Li, C. Xu, Q. Q. Luo, Y. L. Guo, X. M. Wang, *Nat. Commun.* **2021**, *12*, 3813.
[13] J. Oliver-Meseguer, J. R. Cabrero-Antonino, I. Dominguez, A. Leyva-Perez, A. Corma, *Science* **2012**, *338*, 1452–1455.
[14] J. Oliver-Messeguer, L. Liu, S. García-García, C. Canós-Giménez, I. Domínguez, R. Gavara, A. Doménech-Carbó, P. Concepción, A. Leyva-Pérez, A. Corma, *J. Am. Chem. Soc.* **2015**, *137*, 3894–3900.
[15] D. B. Eremin, V. P. Ananikov, *Coord. Chem. Rev.* **2017**, *346*, 2–19.
[16] P. H. Cheong, P. Morganelli, M. R. Luzung, K. N. Houk, F. D. Toste, *J. Am. Chem. Soc.* **2008**, *130*, 4517–4526.
[17] A. S. Hashmi, I. Braun, P. Nosel, J. Schadlich, M. Wieteck, M. Rudolph, F. Rominger, *Angew. Chem. Int. Ed.* **2012**, *51*, 4456–4460.
[18] D. Weber, M. A. Tarselli, M. R. Gagne, *Angew. Chem. Int. Ed.* **2009**, *48*, 5733–5736.
[19] B. Yu, *Acc. Chem. Res.* **2018**, *51*, 507–516.
[20] A. S. Hashmi, *Acc. Chem. Res.* **2014**, *47*, 864–876.
[21] T. J. Brown, D. Weber, M. R. Gagne, R. A. Widenhoefer, *J. Am. Chem. Soc.* **2012**, *134*, 9134–9137.
[22] M. A. Rivero-Crespo, A. Leyva-Pérez, A. Corma, *Chem. - Eur. J.* **2017**, *23*, 1702–1708.
[23] H. Dai, H. Guan, *ACS Catal.* **2018**, *8*, 9125–9130.
[24] S. Hu, T. Shima, Z. Hou, *Nature* **2014**, *512*, 413–415.
[25] T. Murahashi, Y. Hashimoto, K. Chiyoda, M. Fujimoto, T. Uemura, R. Inoue, S. Ogoshi, H. Kurosawa, *J. Am. Chem. Soc.* **2008**, *130*, 8586–8587.
[26] M. Teramoto, K. Iwata, H. Yamaura, K. Kurashima, K. Miyazawa, Y. Kurashige, K. Yamamoto, T. Murahashi, *J. Am. Chem. Soc.* **2018**, *140*, 12682–12686.
[27] M. M. Shoshani, S. A. Johnson, *Nat. Chem.* **2017**, *9*, 1282–1285.
[28] X. L. Pei, A. Pereira, E. S. Smirnova, A. M. Echavarren, *Chem. - Eur. J.* **2020**, *26*, 7309–7313.
[29] S. Li, N. N. Li, X. Y. Dong, S. Q. Zang, T. C. W. Mak, *Chem. Rev.* **2024**, *124*, 7262–7378.
[30] Z. Han, Y. Si, X. Y. Dong, J. H. Hu, C. Zhang, X. H. Zhao, J. W. Yuan, Y. Wang, S. Q. Zang, *J. Am. Chem. Soc.* **2023**, *145*, 6166–6176.
[31] X. Kang, M. Zhu, *Chem. Mater.* **2021**, *33*, 39–62.
[32] X. Zou, X. Kang, M. Zhu, *Chem. Soc. Rev.* **2023**, *52*, 5892–5967.
[33] B. Zhang, C. Xia, J. Hu, H. Sheng, M. Zhu, *Nanoscale* **2024**, *16*, 1526–1538.
[34] H. N. Qin, M. W. He, J. Wang, H. Y. Li, Z. Y. Wang, S. Q. Zang, T. C. W. Mak, *J. Am. Chem. Soc.* **2024**, *146*, 3545–3552.
[35] R. Saito, K. Isozaki, Y. Mizuhata, M. Nakamura, *J. Am. Chem. Soc.* **2024**, *146*, 20930–20936.
[36] C.-C. Li, S. Zhang, J. Tang, R. Jian, Y. Xia, L. Zhao, *Chem. Sci.* **2022**, *13*, 8095–8103.
[37] S. Alvarez, *Dalton Trans.* **2013**, *42*, 8617.
[38] Y. Cao, S. Malola, M. F. Matus, T. Chen, Q. Yao, R. Shi, H. Häkkinen, J. Xie, *Chem* **2021**, *7*, 2227–2244.
[39] Y. Marcus, *Chem. Soc. Rev.* **1993**, *22*, 409–416.
[40] M. J. Kamlet, R. W. Taft, *J. Am. Chem. Soc.* **1976**, *98*, 377–383.
[41] C. Reichardt, T. Welton, *Solvents and Solvent Effects in Organic Chemistry*, Wiley-VCH, Weinheim, Germany **2010**, p. 238.
[42] E. Buncel, R. A. Stairs, *Solvent Effects in Chemistry*, Wiley, Hoboken, NJ **2015**, p. 18.
[43] S. Knoppe, I. Dolamic, T. Bürgi, *J. Am. Chem. Soc.* **2012**, *134*, 13114–13120.
[44] M. Sastry, K. S. Mayya, K. Bandyopadhyay, *Colloids Surf. Physicochem. Eng. Aspects* **1997**, *127*, 221–228.
[45] A. Nasreen, S. R. Adapa, *Heterocycl. Commun.* **2001**, *7*, 501–506.
[46] A. Deb, S. Manna, A. Modak, T. Patra, S. Maity, D. Maiti, *Angew. Chem. Int. Ed.* **2013**, *52*, 9747–9750.
[47] E.-X. Zhang, D.-X. Wang, Q.-Y. Zheng, M.-X. Wang, *Org. Lett.* **2008**, *10*, 2565–2568.
[48] Gaussian 09, Revision E.01, A. V. Marenich, C. J. Cramer, D. G. Truhlar, C. A. Guido, B. Mennucci, G. Scalmani, M. J. Frisch, Gaussian, Inc., Wallingford, CT, **2013**.
[49] F. Neese, F. Wennmohs, U. Becker, C. Riplinger, *J. Chem. Phys.* **2020**, *152*, 224108.
[50] F. Weigend, R. Ahlrichs, *Phys. Chem. Chem. Phys.* **2005**, *7*, 3297.
[51] C. Adamo, V. Barone, *J. Chem. Phys.* **1999**, *110*, 6158–6170.
[52] S. Grimme, J. Antony, S. Ehrlich, H. Krieg, *J. Chem. Phys.* **2010**, *132*, 154104.

[53] A. V. Marenich, C. J. Cramer, D. G. Truhlar, *J. Phys. Chem. B* **2009**, *113*, 6378–6396.
[54] T. Lu, F. Chen, *J. Comput. Chem.* **2012**, *33*, 580–592.
[55] G. M. Sheldrick, *Acta Crystallography. Sect. A* **2008**, *64*, 112–122.
[56] J. L. Atwood, L. J. Barbour, *Cryst. Growth Des.* **2003**, *3*, 3–8.
[57] T. W. Ebbesen, R. Akaba, K. Tokumaru, M. Washio, S. Tagawa, Y. Tabata, *J. Am. Chem. Soc.* **1988**, *110*, 2147–2151.
[58] C.-M. Che, H.-L. Kwong, V. W.-W. Yam, K.-C. Cho, *J. Chem. Soc. Chem. Commun.* **1989**, 885. https://doi.org/10.1039/C39890000885.
[59] V. W.-W. Yam, T.-F. Lai, C.-M. Che, *J. Chem. Soc. Dalton Trans.* **1990**, 3747.
[60] Deposition Numbers 1995296 (**Ag_{13}-A**), 1994912 (**Ag_{13}-M**), and 2344925 (**$(OH)^{Me}$Py-Ag**) contain the supplementary crystallographic datafor this paper. These data are provided free of charge by the jointCambridge Crystallographic Data Centre and Fachinforma-tionszentrum Karlsruhe Access Structures service.

Manuscript received: March 26, 2025
Revised manuscript received: April 19, 2025
Accepted manuscript online: April 21, 2025
Version of record online: April 30, 2025